Available online at www.dergipark.org.tr/en

INTERNATIONAL ADVANCED RESEARCHES
and
ENGINEERING JOURNAL

Journal homepage: www.dergipark.org.tr/en/pub/iarej

e-ISSN: 2618-575X

International Open Access

Volume 08
Issue 03

December, 2024

Research Article

Thermomechanical vibration response of nickel foam nanoplates

Mustafa Eroğlu [a]

[a]*Engineering Faculty, Mechanical Engineering Department, Sakarya University, Sakarya, 54187, Turkey*

ARTICLE INFO

Article history:
Received 22 August 2024
Accepted 19 December 2024
Published 20 December 2024

Keywords:
Foam
Nanoplate
Thermal buckling
Vibration

ABSTRACT

This article studies the buckling properties of nickel foam nanoplate. This research used nonlocal strain gradient elasticity and the new theory of sinusoidal higher-order deformation. After deriving the nanoplate's equations of motion from Hamilton's principle, the Navier technique was used to solve them. Two different kinds of foam models, uniform and symmetric, can be used to depict the nanoplate. Examining the nanoplate's dimensionless fundamental natural frequencies was the study's primary goal. The effects of temperature difference, nonlocal parameters, foam void ratio, and two different kinds of foam were considered in this investigation. In this context, the nanoplate's natural frequency decreases by 23.78% in the symmetric foam model and 51.5% in the uniform foam model as the foam void ratio increases. The research provides valuable insights for the development of nanoelectromechanical systems (NEMS), nanosensors, and transducers intended for high-temperature environments. By analyzing the impact of temperature and foam void ratio on nanoplate stability, the study informs material selection and structural design for applications where performance under thermal stress is critical, such as in aerospace and energy sectors.

1. Introduction

The vibration analysis of nanoplates can be effectively studied through nonlocal viscoelasticity models [1]. These models consider factors like viscoelasticity and piezoelectricity, which are crucial in understanding the dynamic characteristics of nanoscale structures. Researchers have explored the behavior of various nanomaterials like carbon nanotubes under different conditions, such as longitudinal magnetic fields, emphasizing the importance of nonlocal theories in predicting wave propagation and dynamic characteristics [2]. Additionally, using smart materials like self-healing polymer composites has gained attention for repairing microcracks in nanoplates, showcasing the practical applications of advanced materials in maintaining structural integrity [3]. Further research on the size-dependent vibration of nanoplates reinforced with carbon nanotubes under various influences like longitudinal magnetic fields can provide valuable insights into their dynamic behavior [4].

Nanoplates, as nanoscale structures, possess unique properties that can be influenced by various factors, including thermal effects. The thermal properties of nanoplates play a crucial role in their applications, such as in heat dissipation, thermal energy conversion, and thermal stability. The thermal conductivity of nanoplates is a key characteristic that affects their ability to transfer heat efficiently [5]. Similarly, incorporating BN nanoplates into composite materials has been shown to enhance heat conduction and transfer capabilities, as evidenced by increased thermal conductivity and thermal diffusivity [6]. Furthermore, the thermal behavior of nanoplates can impact their photothermal conversion efficiency. Graphite nanoplates, for instance, have been demonstrated to convert solar light into thermal energy through lattice vibrations of the carbon backbone [7]. Moreover, the thermal properties of nanoplates can influence their electrical and thermoelectric performance. For example, the fabrication of Au-Sb_2Te_3 nanoplates with optimized interface barriers and phonon scattering has resulted in synergistically optimal electrical and thermal properties [8]. Additionally, the growth of ultrathin Bi_2Te_3 nanoplates and subsequent fabrication of nanostructured thermoelectric materials have been reported, highlighting the importance of thermal management in enhancing thermoelectric efficiency [9]. Studies have shown that

* Corresponding author. Tel.: *+90-264-295-5587*.
E-mail addresses: mustafaeroglu@sakarya.edu.tr *(M. Eroğlu)*
ORCID: 0000-0002-1429-7656 *(M. Eroğlu)*
DOI: 10.35860/iarej.1537234
© 2024, The Author(s). This article is licensed under the CC BY-NC 4.0 International License (https://creativecommons.org/licenses/by-nc/4.0/).

adding graphene nanoplates to nanofluids can improve thermal efficiency and heat transfer characteristics in heat exchangers [10, 11]. Similarly, metal-containing nanofluids with nanoplates have been investigated for thermal energy storage applications, demonstrating enhanced specific heat due to interfacial layering effects [12].

An expanding field of study, foam nanoplates have great promise for various engineering contexts. Nanoplate structures' vibration properties can be greatly affected by foams. Al-Waily et al. investigated micro aluminum powder-reinforced foam sandwich plates using free vibration analysis [13]. Functionally graded nanoporous metal foam nanoplates showed exceptional fracture toughness and electrical solid conductivities, making them appropriate for thin-film elements [14]. The study focused on free vibration and buckling in the FG porous beam's response to thermal effects and magnetic fields [15]. Zhao et al. investigated the sandwich plates with aluminum foam cores experimentally and numerically [16]. Sun et al. used carbon fiber/epoxy stitched reinforcements with a precisely adjusted fiber volume fraction to strengthen foam core sandwich constructions [17]. Also, aluminum facesheets were utilized with polyurethane and polystyrene foam cores [18].

As demonstrated in a recent study, the use of additives in biodiesel and the coating of tractor engine components can significantly reduce fuel consumption and exhaust emissions, while promoting more environmentally friendly agricultural practices [19]. As investigated in a recent study, blending hexane and water with diesel fuel in ceramic-coated and uncoated diesel engines can improve emission and performance parameters, with the ceramic coating proving to be the most effective factor for all tested parameters [20].

Nanosensors and nanoelectromechanical systems are widely used in high-temperature applications due to nanotechnology's widespread use. To ensure exact measurement and operation of these systems, new designs or configurations, such as the sandwich arrangement, must be developed. This study must make unique contributions due to a dearth of literature. This study examined foam nanoplate thermomechanical vibration to meet the criteria. The nanoplates are nickel foam. The initiative aims to build and test high-temperature nanoplates.

2. Modelling of Foam Nanoplate

The equations of motion for the nanoplate analyzed in this paper were derived using the Hamiltonian approach. This method allows for examining the nanoplate's dynamic behaviour in the temperature environment. Fig. 1 shows the physical depiction of a rectangular nanoplate positioned in the *x*, *y*, *z* coordinate system. The nanoplate consists of a single layer. The dimensions of the nanoplate in the *y* and *x* directions are specified as *a* and *b*, respectively. The thickness is denoted by the variable *h*.

This study investigates the dynamic characteristics of a nanoplate composed exclusively of nickel foam. Fig. 1 displays two distinct varieties of foam nanoplates within this environment. Fig. 1a depicts a homogenous foam model, whereas Fig. 1b shows a foam model with concentrated surface regions. The Young Modulus *E* and densities of the aforementioned models are provided as follows [21–24].

Uniform foam (Fig. 1a):

$$E(z) = E_1(1-\alpha\psi)$$
$$\rho(z) = \rho_1\sqrt{(1-\alpha\psi)}$$
$$\psi = \frac{1}{\alpha} - \frac{1}{\alpha}\left(\frac{2\sqrt{(1-\alpha\psi)}}{\pi} - \frac{2}{\pi} + 1\right)^2 \tag{1}$$

Symmetric foam (Fig. 2a):

$$E(z) = E_1[1-\alpha\cos(\pi z/h)]$$
$$\rho(z) = \rho_1[1-\alpha_d\cos(\pi z/h)]$$
$$\alpha_d = 1-\sqrt{(1-\alpha)} \tag{2}$$

ρ_1 and E_1 denote the density and young modulus of the nickel foam, respectively. The symbol α represents the foam's void ratio.

Uniform foam models represent a consistent distribution of voids throughout the structure, making them suitable for applications requiring isotropic mechanical properties and ease of manufacturing. On the other hand, symmetric foam models account for graded distributions of voids, which are more representative of advanced fabrication techniques, such as additive manufacturing or layer-by-layer deposition.

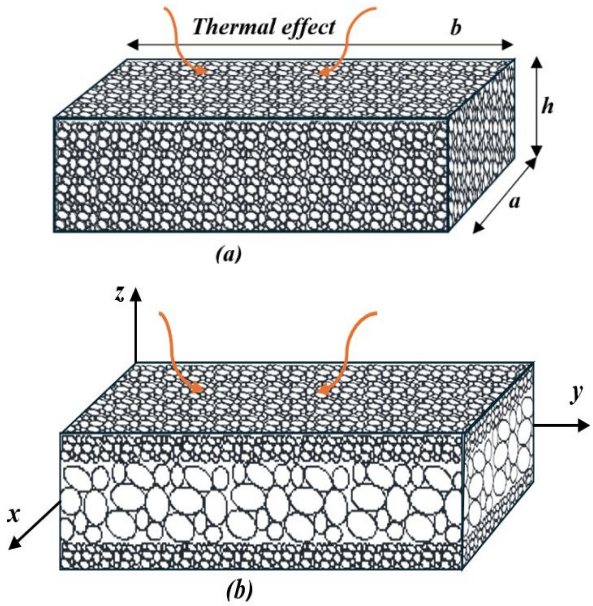

Figure 1. Configuration of nickel nanoplate a) Uniform foam model b) Symmetric foam model

These models offer enhanced control over material properties, allowing for tailored responses to specific operational requirements, such as improved thermal resistance or localized stiffness. By analyzing both models, the study provides a comprehensive understanding of how different foam configurations influence the structural performance of nanoplates, offering insights for designing materials optimized for specific engineering applications.

2.1 The temperature effect on nanoplate

Temperature parameters are necessary as the impact of temperature on the behaviour of the nanoplate is considered. The equation provided describes the non-linear relationship between the material characteristics, such as the temperature-dependent elastic modulus and Poisson's ratio [25].

$$P = P_0(P_{-1}T^{-1} + 1 + P_1T + P_2T^2 + P_3T^3) \tag{3}$$

In this context, the symbol P indicates an ingredient that varies with temperature, whereas P_0 represents the matching material. Table 1 presents the P_{-1}, P_1, P_2, and P_3 values that correlate to the temperature T.

The temperature distribution of the nanoplate in the z direction can be described by the following linear equation. Here, T_1 and T_2 denote the temperature of the lower and upper surfaces, respectively, and the temperature rise is considered to be from T_1 to T_2 [26].

$$T(z) = T_1 + (T_2 - T_1)\left(\frac{h + 2z}{2h}\right) \tag{4}$$

The non-linear temperature rise in the nanoplate is demonstrated by solving the heat transfer equation. The expression is as follows: [27].

$$-\frac{d}{dz}\left(\kappa(z)\frac{dT}{dz}\right) = 0, \qquad T\left(\frac{h}{2}\right) = T_2, \quad T\left(-\frac{h}{2}\right) = T_1 \tag{5}$$

$$T(z) = T_1 + \frac{(T_2 - T_1)}{\int_{-\frac{h}{2}}^{\frac{h}{2}} \frac{1}{\psi(z)} d(z)} \int_{-\frac{h}{2}}^{z} \psi(z)dz \tag{6}$$

Table 1. Coefficients that vary with temperature for Nickel (Ni) characteristics

Property	P_{-1}	P_0	P_1	P_2	P_3
ρ (kg/m^3)	0	8900	0	0	0
E (Pa)	0	223x10^9	-2.79x10^{-4}	3.99x10^{-7}	0
υ	0	0.31	0	0	0
α (1K^{-1})	0	9.9x10^{-6}	8.70x10^{-4}	0	0
ψ (W/mK)	0	58.74	-4.6x10^{-4}	6.67x10^{-7}	-1.52x10^{-10}

2.2 The theory of nonlocal strain gradient theory (NSGT)

Eringen's research suggests that the stress within a body is intrinsically connected to all other locations, and the structure's stiffness is influenced by the material size factor and the nonlocal density [28]. The stress tensors σ and $\boldsymbol{\sigma}^{(\boldsymbol{h})}$ in NSGT are expressed by the following equations [29].

$$\sigma = \int_V \alpha_0(\boldsymbol{x}', \boldsymbol{x}, e_0a)\boldsymbol{C} : \varepsilon'(\boldsymbol{x}')dV' \tag{7a}$$

$$\sigma^{(h)} = l_m^2 \int_V \alpha_1(\boldsymbol{x}', \boldsymbol{x}, e_1a)\boldsymbol{C} : \nabla\varepsilon'(\boldsymbol{x}')dV' \tag{7b}$$

In this context, α_0 and α_1 denote the conventional kernel and nonlocal functions of higher order, while ∇ and C correspond the Laplacian operator (∇=∂/∂x+∂/∂y) and the fourth-order material coefficient, respectively. The terms ∇ε and ε denote the classical strain tensors and the strain gradient, respectively. The symbols e_0 and e_1 represent the nonlocal coefficients, while l_m represents the material size factor. The symbol ":" represents the tensor's double-dot product. The tensor of stress obtained from the Navier equations can be expressed as [29, 30].

$$\sigma^t = \sigma - \nabla^2\sigma^{(1)} \tag{8}$$

Given that the concepts of $\alpha_1(\boldsymbol{x}', \boldsymbol{x}, e_1a)$ and $\alpha_0(\boldsymbol{x}', \boldsymbol{x}, e_0a)$ align with the Ref. [31] and that e_0=e_1=e_0a, using the linear differentiation operator yields the following result.

$$[1 - (e_0a)^2\nabla^2]\,\sigma = \mathbf{C} : \varepsilon, \; [1 - (e_0a)^2\nabla^2]\,\sigma^{(1)} = l_m^2\,\mathbf{C} : \nabla\varepsilon \tag{9}$$

Eq. 9 can be employed to compute the overall stress in the following manner:

$$[1 - (e_0a)^2\nabla^2]\,\sigma = \mathbf{C} : \varepsilon - l_m^2\,\nabla\mathbf{C} : \nabla\varepsilon \tag{10}$$

Stress-strain relations of plate are calculated by Refs. [29, 32]:

$$[1 - (e_0a)^2\nabla^2]\sigma_{xx} = [1 - l_m^2\nabla^2]E(z)\varepsilon_{xx} \tag{11a}$$

$$[1 - (e_0a)^2\nabla^2]\sigma_{yy} = [1 - l_m^2\nabla^2]E(z)\varepsilon_{yy} \tag{11b}$$

$$[1 - (e_0a)^2\nabla^2]\sigma_{xz} = [1 - l_m^2\nabla^2]G(z)\gamma_{xz} \tag{11c}$$

$$[1 - (e_0a)^2\nabla^2]\sigma_{yz} = [1 - l_m^2\nabla^2]G(z)\gamma_{yz} \tag{11d}$$

The equations provided above define the strains and stresses in the y and x directions as σ_{xx}, σ_{yy}, ε_{xx}, and ε_{yy}, respectively. The shear stresses and strains are represented by σ_{xz}, σ_{yz}, and γ_{xz}, γ_{yz}. E(z) and G(z) denote the elasticity and shear modulus, correspondingly. The classical continuum theory's stress-strain relations can be calculated by setting

the nonlocal parameters in these equations to zero [31].

2.3 Kinematic relation

Sinusoidal higher-order shear deformation theory was used in the analysis of this structure consisting of a single-layered rectangular plate [33]. For plane displacements *u* and *v*, u_0 represents extension, w_s represents shear, and w_0 represents bending. To account for bending w_0 and shear w_s components of transverse stresses (σ_{xz}, σ_{yz}, σ_{zz}) and strains (ε_{xz}, ε_{yz}, ε_{zz}), the transverse displacement w is adjusted. Incorporating shear components increases the trigonometric variation of shear stresses (σ_{xz}, σ_{yz}) and strains (ε_{xz}, ε_{yz}) over plate thickness. As to this idea, the nanoplate's displacement field is:

$$\begin{aligned} u(x,y,z,t) &= u_0(x,y,t) - z\frac{\partial w_0(x,y,t)}{\partial x} \\ &\quad - f(z)\frac{\partial w_s(x,y,t)}{\partial x} \\ v(x,y,z,t) &= v_0(x,y,t) - z\frac{\partial w_0(x,y,t)}{\partial y} \\ &\quad - f(z)\frac{\partial w_s(x,y,t)}{\partial y} \\ w(x,y,z,t) &= w_0(x,y,t) + w_s(x,y,t) \\ &\quad + w_{st}(x,y,z,t) \end{aligned} \tag{12}$$

Let's establish the definitions of the *f(z)*, w_{st}, and *g(z)* as follows:

$$\begin{aligned} f(z) &= z - \frac{h}{\pi}\sin\left(\frac{\pi z}{h}\right) \\ w_{st}(x,y,z,t) &= \mathrm{g}(z)\emptyset(x,y,t), \\ g(z) &= cos\,(\frac{\pi z}{h}) \end{aligned} \tag{13}$$

The total displacements represented by the variables *u*, *v*, and *w* in the displacement equations. A midplane of the unshaped plate is represented by the symbols u_0, v_0, and w_0, which stand for in-plane and transverse displacements, respectively. While the w displacement indicates the bending deflection of the plate, the *u* and *v* displacements are linked to its extensional deformation. In terms of the displacement field, the following is a general form for the strain-displacement interactions:

$$\begin{aligned} \begin{Bmatrix} \varepsilon_{xx} \\ \varepsilon_{yy} \\ 2\varepsilon_{xy} \end{Bmatrix} &= \begin{Bmatrix} \varepsilon_{xx}^{(0)} \\ \varepsilon_{yy}^{(o)} \\ \gamma_{xy}^{(0)} \end{Bmatrix} + z\begin{Bmatrix} \varepsilon_{xx}^{(b)} \\ \varepsilon_{yy}^{(b)} \\ \gamma_{xy}^{(s)} \end{Bmatrix} \\ \begin{Bmatrix} 2\varepsilon_{xz} \\ 2\varepsilon_{yz} \end{Bmatrix} &= g(z)\begin{Bmatrix} \gamma_{xz}^{(0)} \\ \gamma_{yz}^{(0)} \end{Bmatrix} \\ \varepsilon_{zz} &= g'(z)\varepsilon_{zz}^{(0)} \end{aligned} \tag{14}$$

The strain components are as follows:

$$\begin{aligned} \begin{Bmatrix} \varepsilon_{xx}^{(0)} \\ \varepsilon_{yy}^{(0)} \\ \gamma_{xy}^{(0)} \end{Bmatrix} &= \begin{Bmatrix} \dfrac{\partial u_0}{\partial x} \\ \dfrac{\partial v_0}{\partial y} \\ \dfrac{\partial u_0}{\partial y} + \dfrac{\partial v_o}{\partial x} \end{Bmatrix}, \begin{Bmatrix} \varepsilon_{xx}^{(b)} \\ \varepsilon_{yy}^{(b)} \\ \gamma_{xy}^{(b)} \end{Bmatrix} \\ &= \begin{Bmatrix} -\dfrac{\partial^2 w_0}{\partial x^2} \\ -\dfrac{\partial^2 w_0}{\partial y^2} \\ -2\dfrac{\partial^2 w_0}{\partial x \partial y} \end{Bmatrix} \\ \begin{Bmatrix} \gamma_{xz}^{(0)} \\ \gamma_{yz}^{(o)} \end{Bmatrix} &= \begin{Bmatrix} \left(1 - f'(z)\right)\dfrac{\partial w_s}{\partial x} + g(z)\dfrac{\partial \emptyset}{\partial x} \\ \left(1 - f'(z)\right)\dfrac{\partial w_s}{\partial y} + g(z)\dfrac{\partial \emptyset}{\partial y} \end{Bmatrix} \\ &= \begin{Bmatrix} g(z)\left(\dfrac{\partial w_s}{\partial x} + \dfrac{\partial \emptyset}{\partial x}\right) \\ g(z)\left(\dfrac{\partial w_s}{\partial y} + \dfrac{\partial \emptyset}{\partial y}\right) \end{Bmatrix} \\ \varepsilon_{zz}^{(0)} &= \emptyset \end{aligned} \tag{15}$$

The stresses can be obtained from the constitutive relations using the given formula.

$$\begin{Bmatrix} \sigma_x \\ \sigma_y \\ \sigma_z \\ \sigma_{xy} \\ \sigma_{xz} \\ \sigma_{yz} \end{Bmatrix} = \begin{bmatrix} C_{11} & C_{12} & C_{13} & 0 & 0 & 0 \\ C_{12} & C_{22} & C_{23} & 0 & 0 & 0 \\ C_{13} & C_{23} & C_{33} & 0 & 0 & 0 \\ 0 & 0 & 0 & C_{66} & 0 & 0 \\ 0 & 0 & 0 & 0 & C_{55} & 0 \\ 0 & 0 & 0 & 0 & 0 & C_{44} \end{bmatrix} \begin{Bmatrix} \varepsilon_x \\ \varepsilon_y \\ \varepsilon_z \\ \gamma_{xy} \\ \gamma_{xz} \\ \gamma_{yz} \end{Bmatrix} \tag{16}$$

which are defined as the three-dimensional elastic constants C_{ij}

$$\begin{aligned} C_{11} = C_{22} = C_{33} &= \frac{(1-v)E}{(1-2v)(1+v)} \\ C_{12} = C_{13} = C_{23} &= \frac{vE}{(1-2v)(1+v)} \\ C_{44} = C_{55} = C_{66} &= \frac{E}{2(1+v)} \end{aligned} \tag{17}$$

Rewriting the constitutive relations

$$\begin{Bmatrix} \sigma_x \\ \sigma_y \\ \sigma_{xy} \\ \sigma_{yz} \\ \sigma_{xz} \end{Bmatrix} = \frac{E}{1-v^2}\begin{bmatrix} 1 & v & 0 & 0 & 0 \\ v & 1 & 0 & 0 & 0 \\ 0 & 0 & \dfrac{(1-v)}{2} & 0 & 0 \\ 0 & 0 & 0 & \dfrac{(1-v)}{2} & 0 \\ 0 & 0 & 0 & 0 & \dfrac{(1-v)}{2} \end{bmatrix} \begin{Bmatrix} \varepsilon_x \\ \varepsilon_y \\ \gamma_{xy} \\ \gamma_{yz} \\ \gamma_{xz} \end{Bmatrix} \tag{18}$$

where nanoplate Young's modulus is E and Poisson's ratio is v. For simplicity's sake, we'll assume that Poisson's ratio v is constant, since it has a negligible effect on nanoplate responses.

The strain energy

$$U = \frac{1}{2}\int_A \int_{-h/2}^{h/2} \left(\sigma_x \varepsilon_x + \sigma_y \varepsilon_y + \sigma_z \varepsilon_z + \sigma_{xy}\gamma_{xy} + \sigma_{xz}\gamma_{xz} + \sigma_{yz}\gamma_{yz}\right) dA dz \tag{19}$$

The strain energy can be rewritten as below:

$$U = \frac{1}{2}\int_A \left[N_x \frac{\partial u}{\partial x} - M_x^b \frac{\partial^2 w_b}{\partial x^2} + N_y \frac{\partial v}{\partial y} - M_y^b \frac{\partial^2 w_b}{\partial y^2} + R_z w_z + N_{xy}\left(\frac{\partial u}{\partial y} + \frac{\partial v}{\partial x}\right) - 2M_{xy}^b \frac{\partial^2 w_b}{\partial x\, \partial y} + Q_z\left(\frac{\partial w_s}{\partial x} + \frac{\partial w_z}{\partial x}\right) + Q_y\left(\frac{\partial w_s}{\partial y} + \frac{\partial w_z}{\partial y}\right)\right] \tag{20}$$

as the stress resultants N, M, Q, and R are defined by

$$\begin{aligned} \left(N_x, N_y, N_{xy}\right) &= \int_{-\frac{h}{2}}^{\frac{h}{2}} \left(\sigma_x, \sigma_y, \sigma_{xy}\right) dz \\ \left(M_x^b, M_y^b, M_{xy}^b\right) &= \int_{-h/2}^{h/2} \left(\sigma_x, \sigma_y, \sigma_{xy}\right) z dz \\ \left(Q_x, Q_y\right) &= \int_{-\frac{h}{2}}^{\frac{h}{2}} \left(\sigma_{xz}, \sigma_{yz}\right) g(z) dz \\ R_z &= \int_{-h/2}^{h/2} \sigma_z g'(z) dz \end{aligned} \tag{21}$$

Stress results is given as below:

$$\begin{aligned} N_x &= A_{11}\frac{\partial u}{\partial x} + A_{12}\frac{\partial v}{\partial y} - B_{11}\frac{\partial^2 w_b}{\partial x^2} - B_{12}\frac{\partial^2 w_b}{\partial y^2} + X_{13} w_z \\ N_y &= A_{12}\frac{\partial u}{\partial x} + A_{22}\frac{\partial v}{\partial y} - B_{12}\frac{\partial^2 w_b}{\partial x^2} - B_{22}\frac{\partial^2 w_b}{\partial y^2} + X_{23} w_z \\ N_{xy} &= A_{66}\left(\frac{\partial u}{\partial y} + \frac{\partial v}{\partial x}\right) - 2B_{66}\frac{\partial^2 w_b}{\partial x\, \partial y} \\ M_x^b &= B_{11}\frac{\partial u}{\partial x} + B_{12}\frac{\partial v}{\partial y} - D_{11}\frac{\partial^2 w_b}{\partial x^2} - D_{12}\frac{\partial^2 w_b}{\partial y^2} + Y_{13} w_z \\ M_y^b &= B_{12}\frac{\partial u}{\partial x} + B_{22}\frac{\partial v}{\partial y} - D_{12}\frac{\partial^2 w_b}{\partial x^2} - D_{22}\frac{\partial^2 w_b}{\partial y^2} + Y_{23} w_z \\ M_{xy}^b &= B_{66}\left(\frac{\partial u}{\partial y} + \frac{\partial v}{\partial x}\right) - 2D_{66}\frac{\partial^2 w_b}{\partial x\, \partial y} \\ R_z &= X_{13}\frac{\partial u}{\partial x} + X_{23}\frac{\partial v}{\partial y} - Y_{13}\frac{\partial^2 w_b}{\partial x^2} - Y_{23}\frac{\partial^2 w_b}{\partial y^2} + Z_{33} w_z \end{aligned} \tag{22}$$

where

$$\begin{aligned} \left(A_{ij}, B_{ij}, D_{ij}, H_{ij}^s\right) &= \int_{-\frac{h}{2}}^{\frac{h}{2}} (1, g^2, z, f, z^2, fz, f^2) C_{ij} dz \\ \left(X_{ij}, Y_{ij}, Z_{ij}\right) &= \int_{-h/2}^{h/2} (g', g'z, g'f, g'^2) C_{ij} dz \end{aligned} \tag{23}$$

Work is done by externally transverse loads q by the use of

$$V = -\int_A q(w_b + w_s + g w_z) dA \tag{24}$$

The kinetic energy;

$$K = \frac{1}{2}\int_A \int_{-h/2}^{h/2} \rho(\dot{u}_1^2 + \dot{u}_2^2 + \dot{u}_3^2) dA dz \tag{25}$$

where ρ is the effective mass density of plates and the dot-superscript convention shows the differentiation concerning the time variable t. The equations of motion are determined using Hamilton's principle. The principle can be indicated analytically in one approach as

$$\int_0^T \delta(U + V - K) dt = 0 \tag{26}$$

δ is the variational operator.

To obtain the following motion equations, we take the U, V, and K expressions, and then gather the coefficients of (δ_u, δ_v, δ_{wb}, δ_{ws}, δ_{wz}).

$$\begin{aligned} \delta u &: \frac{\partial N_x}{\partial x} + \frac{\partial N_{xy}}{\partial y} = I_0 \ddot{u} - I_1 \frac{\partial \ddot{w}_b}{\partial x} - J_1 \frac{\partial \ddot{w}_s}{\partial x} \\ \delta v &: \frac{\partial N_{xy}}{\partial x} + \frac{\partial N_y}{\partial y} = I_0 \ddot{v} - I_1 \frac{\partial \ddot{w}_b}{\partial y} - J_1 \frac{\partial \ddot{w}_s}{\partial y} \\ \delta w_b &: \frac{\partial^2 M_x^b}{\partial x^2} + 2\frac{\partial^2 M_{xy}^b}{\partial x\, \partial y} + \frac{\partial^2 M_y^b}{\partial y^2} + q = I_0(\ddot{w}_b + \ddot{w}_s) + J_0 \ddot{w}_z + I_1\left(\frac{\partial \ddot{u}}{\partial x} + \frac{\partial \ddot{v}}{\partial y}\right) - I_2 \nabla^2 \ddot{w}_b - J_2 \nabla^2 \ddot{w}_s \\ \delta w_s &: \frac{\partial Q_{xz}}{\partial x} + \frac{\partial Q_{yz}}{\partial y} + q = I_0(\ddot{w}_b + \ddot{w}_s) + J_0 \ddot{w}_z + J_1\left(\frac{\partial \ddot{u}}{\partial x} + \frac{\partial \ddot{v}}{\partial y}\right) - J_2 \nabla^2 \ddot{w}_b - K_2 \nabla^2 \ddot{w}_s \end{aligned} \tag{27}$$

$$\delta w_z: \frac{\partial Q_{xz}}{\partial x} + \frac{\partial Q_{yz}}{\partial y} - R_z + gq = J_0(\ddot{w}_b + \ddot{w}_s) + K_0 \ddot{w}_z$$

2.4 Analytical Solution

By using Navier's approach with simple boundary conditions, we may estimate displacements *u(x,t)*, *w(x,t)* and *ϕ(x,t)* with a periodic solution in time.

$$\begin{aligned} u(x,y,t) &= \sum_{m=1}^{\infty}\sum_{n=1}^{\infty} U_{mn} e^{i\omega_n t} \cos\alpha x \sin\beta y \\ v(x,y,t) &= \sum_{m=1}^{\infty}\sum_{n=1}^{\infty} V_{mn} e^{i\omega_n t} \sin\alpha x \cos\beta y \\ w_b(x,y,t) &= \sum_{m=1}^{\infty}\sum_{n=1}^{\infty} W_{bmn} e^{i\omega_n t} \sin\alpha x \sin\beta y, \\ w_s(x,y,t) &= \sum_{m=1}^{\infty}\sum_{n=1}^{\infty} W_{smn} e^{i\omega_n t} \sin\alpha x \sin\beta y \\ w_z(x,y,t) &= \sum_{m=1}^{\infty}\sum_{n=1}^{\infty} W_{zmn} e^{i\omega_n t} \sin\alpha x \sin\beta y \end{aligned} \tag{28}$$

$$\beta = \left(\frac{n\pi}{L}\right) \qquad \alpha = \left(\frac{m\pi}{L}\right)$$

The coefficients (U_{mn}, V_{mn}, W_{bmn}, W_{smn}, W_{zmn}) and natural frequency ω_n are represented. Eq. (28) solves for U_n, W_n, and Φ_n at x=0 and x=L, satisfying both classical and non-classical boundary conditions.

The closed-form answers are derived below:

$$\left(\begin{bmatrix} s_{11} & s_{12} & s_{13} & s_{14} & s_{15} \\ s_{12} & s_{22} & s_{23} & s_{24} & s_{25} \\ s_{13} & s_{23} & s_{33} & s_{34} & s_{35} \\ s_{14} & s_{24} & s_{34} & s_{44} & s_{45} \\ s_{15} & s_{25} & s_{35} & s_{45} & s_{55} \end{bmatrix} - \omega^2 \begin{bmatrix} m_{11} & 0 & m_{13} & m_{14} & 0 \\ 0 & m_{22} & m_{23} & m_{24} & 0 \\ m_{13} & m_{23} & m_{33} & m_{34} & m_{35} \\ m_{14} & m_{24} & m_{34} & m_{44} & m_{45} \\ 0 & 0 & m_{35} & m_{45} & m_{55} \end{bmatrix}\right) \begin{Bmatrix} U_{mn} \\ V_{mn} \\ W_{bmn} \\ W_{smn} \\ W_{zmn} \end{Bmatrix} = 0 \tag{29}$$

In Eq. (28), i is the imaginary unit. The symbol ω_n represents the nth natural vibration frequencies.

$$(\mathbf{S} - \omega_n^2 \mathbf{M})\mathbf{d} = 0 \tag{30}$$

For this context, the vector of defined unknowns is $\mathbf{d} = \{U_n \quad W_n \quad \Phi_n\}^{\boldsymbol{T}}$. Matrix **S** symbolizes stiffness and **M** mass. These matrices' coefficients are in Appendix A.

2.2 Verification

Table 2. Comparison of dimensionless frequency $\overline{w}$ in SSSS rectangular plates

Mode	Ref. [35]	Ref. [36]	Present Study
(1,1)	10.024	9.525	10.158
(2,2)	32.571	28.762	31.853
(3,3)	66.284	50.966	63.356
(4,4)	104.006	131.186	112.967
(5,5)	129.647	139.106	134.589

A comparative study was managed to verify the current methodology by comparing the central deflections of rectangular and square plates using three nonlocal plate theories. This study builds upon previous research [34]. The center deflection $\overline{w}$ is standardized by employing the equation for the point load q_0 and the uniform load Q_0.

$$\overline{w} = -w\left(\frac{Eh^2}{q_0 a^4}\right)10^2, \overline{w} = -w\left(\frac{Eh^2}{Q_0 a^4}\right)10^2 \tag{31}$$

The plate parameters are b, h, E, and ρ, signifying length, height, elasticity modulus, and density. Table 2 presents a comparison of central deflections for SSSS isotropic plates with a length of a=10, modulus of elasticity E=30x10^6 MPa, and Poisson's ratio v=0.3, under a point load q_0=1N. The table includes the central deflections obtained using various theories.

To assess the correctness of the suggested method, the findings were compared with data from the literature Ref. [35] and Ref. [36]. Table 2 demonstrates a strong concordance between the findings of this investigation and those of the comparative studies. This validates the precision and dependability of the suggested procedure. The method demonstrates high accuracy in both analytical and numerical approaches. This comparison demonstrates that the suggested model exhibits competitive performance relative to existing methods in the literature and is suitable for safe application in engineering contexts.

3. Results

This study examined the fundamental dimensionless natural frequencies of the nanoplate at various temperatures. The nanoplate is composed of Nickel materials. In Fig. 1, The nanoplate can be classified into two unique foam types: the uniform foam model and the symmetric foam model. The frequencies are provided for foam void ratios (FVR) and two distinct foam types. The length of the nanoplate is b=500 nm, and its height is one-tenth of its length. The width of the plate is also the same as its length. In addition, the nanoplate was subjected to extreme temperature variations from all directions.

Fig. 2 illustrates the relationship between the fundamental natural frequencies of the nanoplate and both the foam void

ratio (FVR) and temperature variations. As the FVR rises, the natural frequencies decrease, indicating a reduction in the nanoplate's stiffness and structural stability. Similarly, as the ΔT rises, natural frequencies diminish further, eventually reaching zero at ΔT=3484, signaling the onset of buckling. This behavior underscores the critical role of thermal effects and material porosity in the structural integrity of nanoplates. Specifically, Fig. 2a shows that for a uniform foam model at ΔT=0, the dimensionless natural frequency of the nanoplate is $\lambda_{(1,1)}$=6.39, 5.34, 4.45, and 3.10 for foam void ratio α=0, 0.3, 0.6, and 0.9, respectively. This corresponds to a 51.5% reduction in the natural frequency as the FVR increases from 0 to 0.9, reflecting a significant weakening of the nanoplate's dynamic response due to increased void content. Fig. 2b highlights the symmetric foam model under the same FVR range, where the natural frequencies are $\lambda_{(1,1)}$=6.39, 5.69, 5.16, and 4.87 for α=0, 0.3, 0.6, and 0.9, respectively. Here, the reduction in natural frequency is comparatively lower at 23.78%, suggesting better retention of structural stability under increased FVRs. In Fig. 2c, the dependence of the natural frequencies on temperature variations for both foam types is presented at α=0.6. At ΔT=0, the natural frequency is $\lambda_{(1,1)}$=4.45 for uniform foam and 5.16 for symmetric foam. The plots indicate that the symmetric foam model exhibits higher frequency stability under temperature changes, while the uniform foam model is more susceptible to thermal effects. These observations highlight the importance of foam type and thermal considerations in designing nanoplates for applications requiring high stability, such as in thermal environments or precision instruments. The dimensionless natural frequencies of the nanoplate are investigated in Fig. 3, which illustrates the effect of α and temperature difference ΔT on its mechanical behavior. The analysis includes four different temperature variances and two types of foam. From the graphs, it is clear that the natural frequency of the nanoplate decreases as both the temperature difference and foam void ratio increase. The decrease in natural frequency with higher temperature differences can be attributed to the increased thermal stresses that reduce the structural stiffness of the nanoplate. In Fig. 3a, the natural frequency of the nanoplate for the uniform foam type at ΔT=0, 300, 600, and 1000 is $\lambda_{(1,1)}$=6.39, 6.1, 5.79, and 5.36, respectively. At a foam void ratio of 0.9, the frequencies are $\lambda_{(1,1)}$=3.1, 2.96, 2.81, and 2.6, showing a significant decrease of approximately 51% as the foam void ratio increases. The trend in Fig. 3b further emphasizes this, with a considerable decrease in the nanoplate's natural frequency as the foam void ratio increases. Fig. 3c compares the natural frequencies of uniform and symmetric foam types at a temperature difference of 600. The natural frequency values for both foam types are consistent when the α is zero, which signifies a solid material with no voids. As the foam void ratio increases, the natural frequency values decrease.

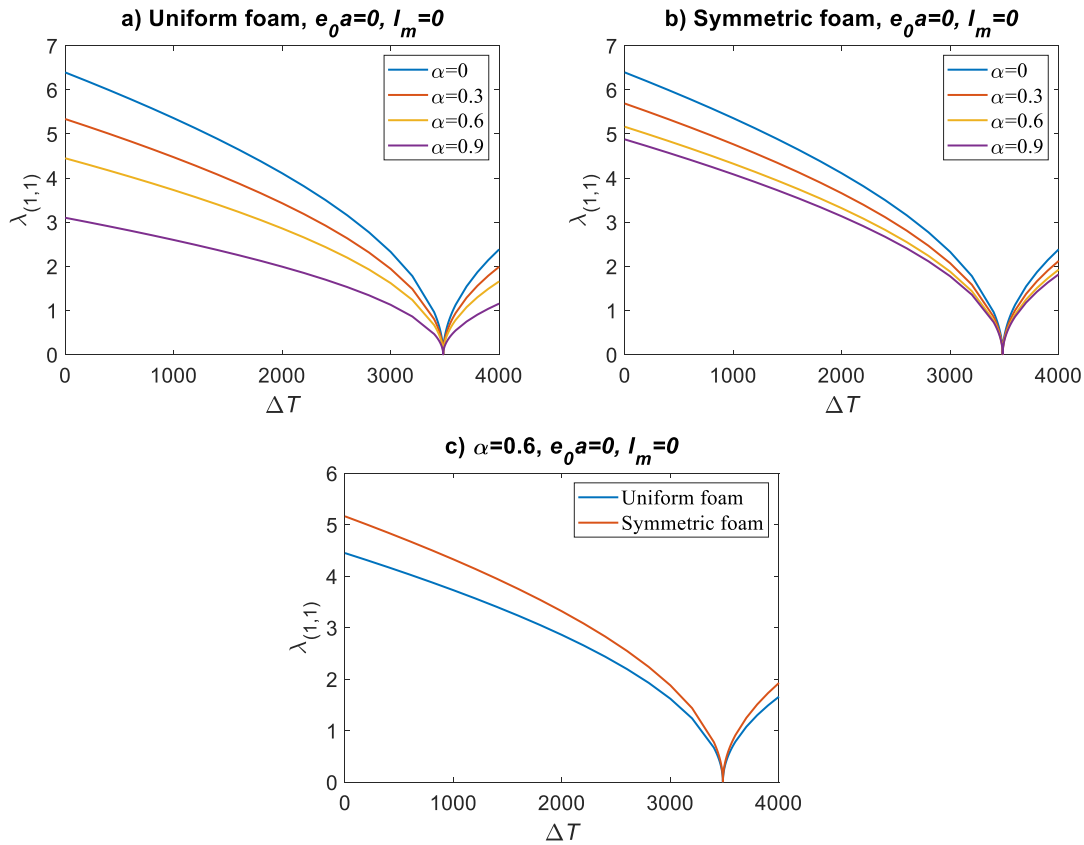

Figure. 2. Changing of the $\lambda_{(1,1)}$ depending on the ΔT and four distinct foam void ratios (α=0, 0.3, 0.6, 0.9)

For α=0, the natural frequency for both foam types is 5.79, whereas at α=0.9, the frequencies are 2.8 for uniform foam and 4.41 for symmetric foam. This demonstrates that while both foam types experience a reduction in natural frequency with increasing void ratio, the symmetric foam shows a comparatively smaller decrease, indicating that its structure might retain more stiffness and stability than the uniform foam under thermal and mechanical loading.

Figure 4 analyzes the effect of altering the temperature difference on the intrinsic natural frequency of the nanoplate. This is accomplished by analyzing four nonlocal parameters designated as e_0a=0, 1, 2, and 4. The graphical representations indicate that an increase in the nonlocal parameter and ΔT leads to a decrease in the natural frequency. Furthermore, it is crucial to note that even with a temperature differential of ΔT=3485, the nanoplate continues to undergo buckling. Analysis of Fig. 4a reveals that augmenting the nonlocal parameter from e_0a=0 to e_0a=4 nm² leads to a 25.28% reduction in the natural frequency, decreasing from λ=5.34 to λ=3.99. In Fig. 4b, the λ of the nanoplate is ascertained to be 5.69, with a nonlocal parameter e_0a of 0 and a ΔT of 0. Fig. 4c presents a comparative analysis of two different types of foam based on a singular nonlocal parameter. The variation in the fundamental frequencies of the nanoplate, seen in Fig. 5, is obtained by analyzing four distinct material size factors (l_m=0, 1, 2, and 4) alongside the temperature differential. Data analysis reveals that the dimensions of the material significantly influence the natural frequencies. In Fig. 5a, with parameters l_m=0 and ΔT=0, the natural frequency is determined to be λ=5.34. However, when the value of l_m is adjusted to 4 nm², the natural frequency rises to λ=7.14. Notably, when the material size grows, the natural frequency experiences an estimated 34% increase. In Fig. 5b, the natural frequencies of the symmetric foam model rise by around 33% with an increase in the material size factor. Furthermore, as the ΔT increases, the inherent frequencies across all dimensions of the material decrease.

At a temperature difference of 3484, the natural frequency values diminish to zero, leading to buckling. Moreover, when the nonlocal parameter increases in the graph above, the natural frequency of the nanoplate decreases, whereas it increases with a rise in material size factor. The graph in Fig. 5c depicts a comparison between two different types of foam, depending on a single factor of material size.

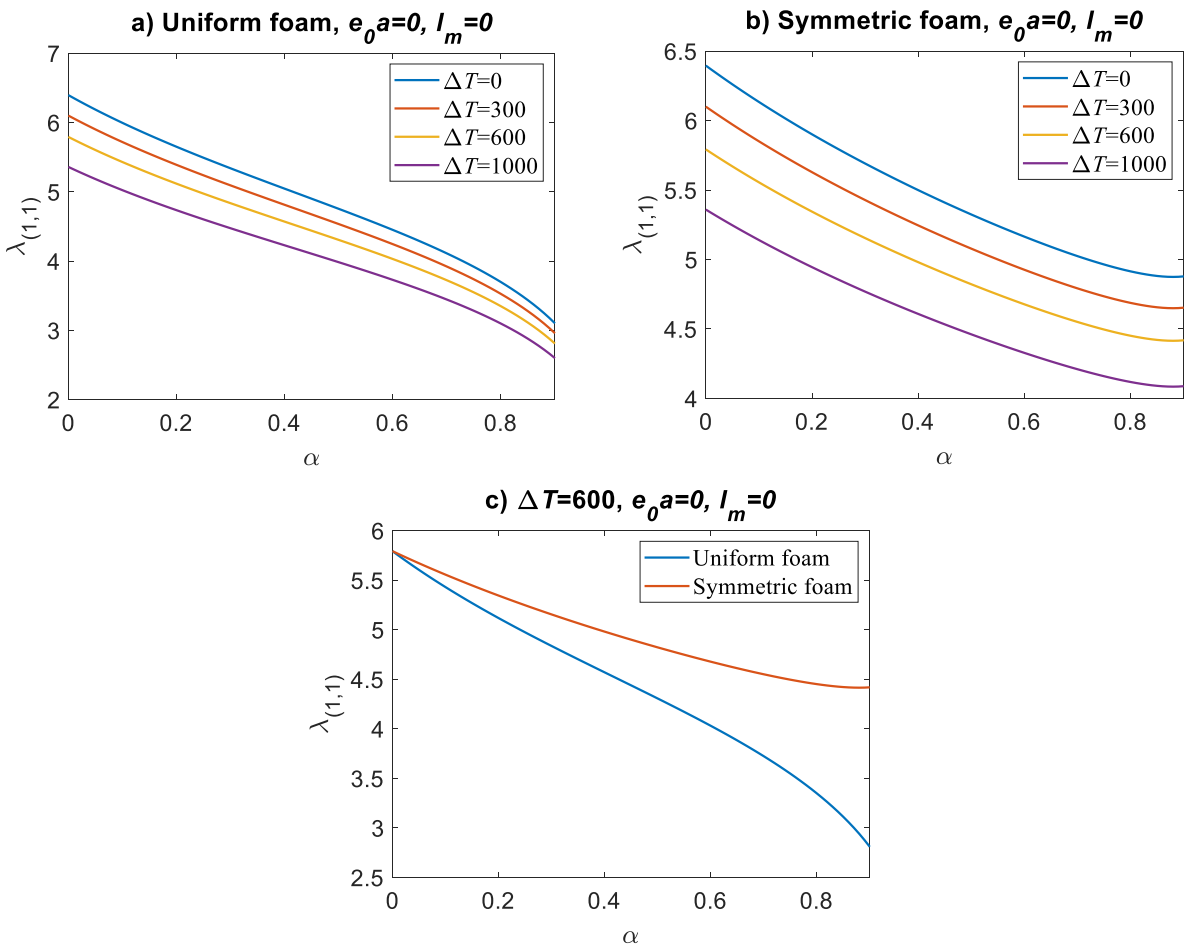

Figure 3. Changing of the $\lambda_{(1,1)}$ depending on the foam void ratio α and four distinct ΔT (ΔT=0, 300, 600, 1000)

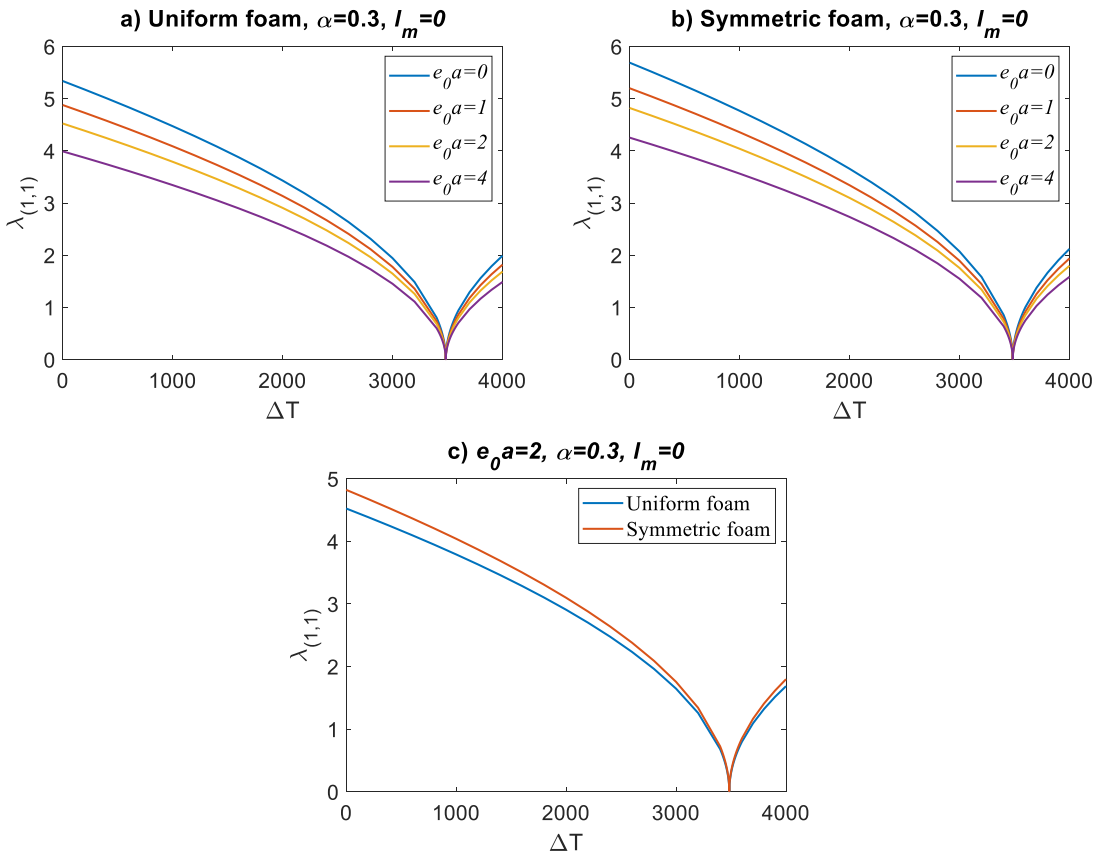

Figure 4 . Changing of the $\lambda_{(1,1)}$ depending on the ΔT and four distinct nonlocal parameters (e_0a=0, e_0a=0.3, e_0a=0.6, e_0a=0.9)

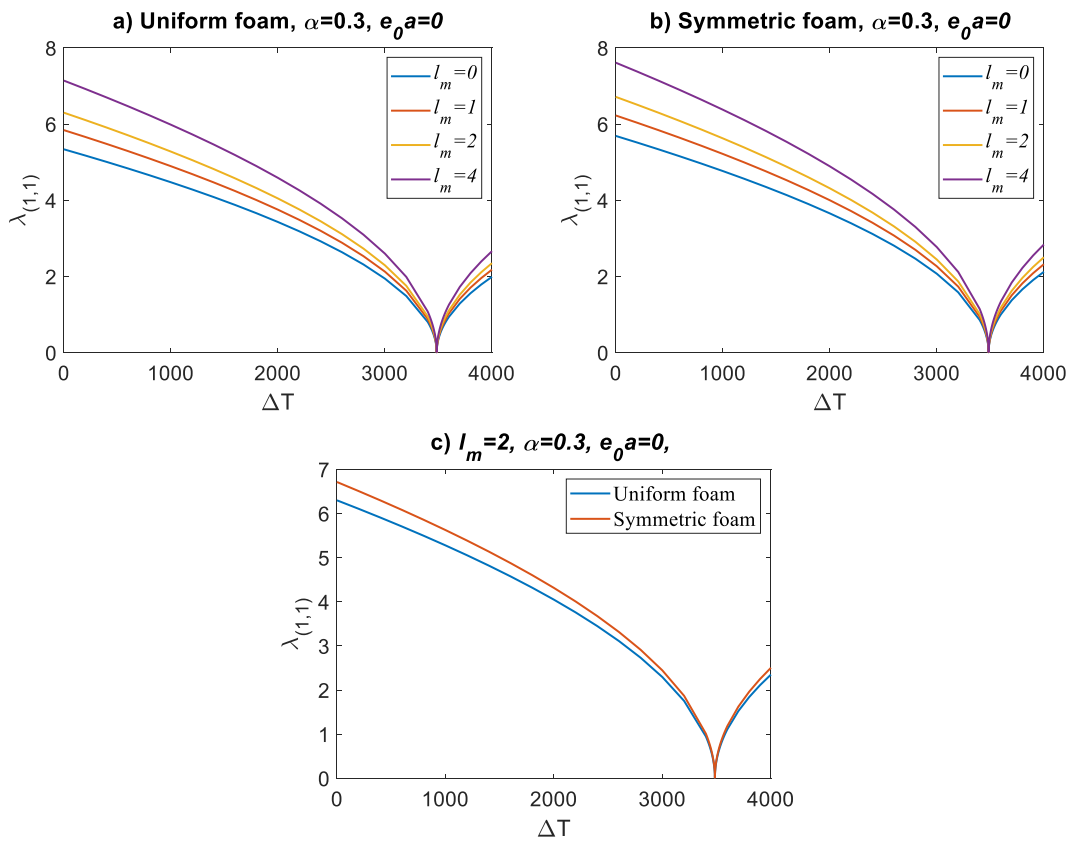

Figure 5 Changing of the $\lambda_{(1,1)}$ depending on the ΔT and four distinct material size factors (l_m=0, l_m=0.3, l_m=0.6, l_m=0.9)

3. Conclusions

In the current study, the buckling characteristics of a nanoplate made of nickel are investigated, with a particular focus on how temperature changes influence the buckling process. The study also examines the modeling of two distinct foam structures, the uniform and symmetric foam models, and explores how their material properties impact buckling behavior under thermal loading. Trigonometric functions are utilized to determine the thermal buckling characteristics of nanoplates within the framework of sinusoidal higher-order shear deformation theory.

A thorough analysis was conducted on the effects of several parameters, including temperature variations, foam type, foam void ratio, and the influence of material properties such as thermal expansion coefficients and stiffness. Nonlocal and material size factors were considered, highlighting their role in the nanoplate's stability under temperature-induced stresses. The findings provide valuable insights into the interplay between temperature changes and material characteristics, offering a deeper understanding of their impact on buckling behavior.

The results are consistent with previous studies that examined the influence of foam structures on the dynamic response and thermal stability of nanoplates. Similar to the findings in studies on nanocomposites and nanostructured materials, the present work emphasizes the importance of material properties, such as thermal expansion coefficients, in governing the thermomechanical behavior of foam nanoplates. This study contributes to the ongoing research on high-temperature applications and highlights the potential of foam nanoplates for engineering applications, especially in systems exposed to thermal loads.

Additionally, future studies may explore using advanced composite materials and hybrid nanostructures to investigate their potential for improving the mechanical properties and thermal stability of foam nanoplates under extreme conditions. Finally, exploring the effects of additional environmental factors such as humidity and pressure could provide a more comprehensive understanding of the nanoplate's performance in real-world applications.

•In the context of the symmetric foam model, the nanoplate's natural frequency experiences a decrease of 23.78% as the FVR grows. In contrast, the uniform foam model results in a more significant decrease of 51.5% in the nanoplate's natural frequency.

•When the FVR is 0, the component has no empty spaces. As the FVR increases, the natural frequency decreases.

•An observed correlation exists between the rise in the nonlocal parameter and the temperature difference, reflected in the reduction of the natural frequency.

•The natural frequency of the nanoplate reduces as the nonlocal parameter increases, whereas it increases when the material size factor is included in the equation.

Declaration

The author declared no potential conflicts of interest with respect to the research, authorship, and/or publication of this article. The author also declared that this article is original and was prepared in accordance with international publication and research ethics, and ethical committee permission or any special permission is not required.

Author Contributions

Mustafa Eroğlu developed the methodology, performed the simulation codes, and wrote the manuscript.

References

1. Ghorbanpour-Arani, A.H., Rastgoo, A., Sharafi, M.M., Kolahchi, R., and Ghorbanpour Arani, A., *Nonlocal viscoelasticity based vibration of double viscoelastic piezoelectric nanobeam systems*. Meccanica, 2016. **51**(1): p. 25–40.
2. Ghorbanpour-Arani, A.H., Rastgoo, A., Hafizi Bidgoli, A., Kolahchi, R., and Ghorbanpour Arani, A., *Wave propagation of coupled double-DWBNNTs conveying fluid-systems using different nonlocal surface piezoelasticity theories*. Mechanics of Advanced Materials and Structures, 2017. **24**(14): p. 1159–1179.
3. Ghorbanpour Arani, A., Miralaei, N., Farazin, A., and Mohammadimehr, M., *An extensive review of the repair behavior of smart self-healing polymer matrix composites*. Journal of Materials Research, 2023. **38**(3): p. 617–632.
4. Ghorbanpour Arani, A., Haghparast, E., and Ghorbanpour Arani, A.H., *Size-dependent vibration of double-bonded carbon nanotube-reinforced composite microtubes conveying fluid under longitudinal magnetic field*. Polymer Composites, 2014. **37**(5): p. 1375–1383.
5. Meng, M., Yuan, Y., Liu, J.G., Geng, C., and Xu, S., *Phosphor-Converted LEDs Based on CdSe/CdS Quantum Rod–BN Nanoplate Assembly*. ACS Applied Nano Materials, 2024. **7**(12): p. 14719–14726.
6. Lin, Y., Qin, C., Fang, L., Wang, J., and Li, D., *Colored Polymeric Films with a Bilayer Porous Design for Efficient Subambient Radiative Cooling*. ACS Applied Polymer Materials, 2024. **6**(1): p. 722–731.
7. Zhao, X., Tang, Y., Wang, J., Li, Y., Li, D., Zuo, X., and Yang, H., *Visible Light Locking in Mineral-Based Composite Phase Change Materials Enabling High Photothermal Conversion and Storage*. ACS Applied Materials & Interfaces, 2023. **15**(42): p. 49132–49145.
8. Kohashi, K., Okano, Y., Tanisawa, D., Kaneko, K., Miyake, S., and Takashiri, M., *Surface Modification of Bi2Te3 Nanoplates Deposited with Tin, Palladium, and Tin/Palladium Using Electroless Deposition*. Crystals, 2024. **14**(2): p. 132.
9. Son, J.S., Choi, M.K., Han, M.-K., Park, K., Kim, J.-Y., Lim, S.J., Oh, M., Kuk, Y., Park, C., Kim, S.-J., and Hyeon, T., *n-Type Nanostructured Thermoelectric Materials Prepared from Chemically Synthesized Ultrathin Bi2Te3 Nanoplates*. Nano Letters, 2012. **12**(2): p. 640–647.
10. Zhu, H., and Fan, L., *Nanofluids effect on the overall transfer coefficients change mechanism analysis*.

Energy Science & Engineering, 2023. **11**(2): p. 4481–4492.

11. Zolfalizadeh, M., Zeinali Heris, S., Pourpasha, H., Mohammadpourfard, M., and Meyer, J.P., *Experimental Investigation of the Effect of Graphene/Water Nanofluid on the Heat Transfer of a Shell-and-Tube Heat Exchanger*. International Journal of Energy Research, 2023. **2023**(1): p. 1–16.
12. Carrillo-Berdugo, I., Midgley, S.D., Grau-Crespo, R., Zorrilla, D., and Navas, J., *Understanding the Specific Heat Enhancement in Metal-Containing Nanofluids for Thermal Energy Storage: Experimental and Ab Initio Evidence for a Strong Interfacial Layering Effect*. ACS Applied Energy Materials, 2020. **3**(9): p. 9246–9256.
13. Al-Waily, M., Raad, H., and Njim, E.K., *Free Vibration Analysis of Sandwich Plate-Reinforced Foam Core Adopting Micro Aluminum Powder*. Physics and Chemistry of Solid State, 2022. **23**(4): p. 659–668.
14. Wang, Y., and Zhang, Z., *Non-Local Buckling Analysis of Functionally Graded Nanoporous Metal Foam Nanoplates*. Coatings, 2018. **8**(11): p.389.
15. Eroğlu, M., Esen, İ., and Koç, M.A., T*hermal vibration and buckling analysis of magneto-electro-elastic functionally graded porous higher-order nanobeams using nonlocal strain gradient theory*. Acta Mechanica, 2024. **235**(2): p. 1175–1211.
16. Zhao, N., Ye, R., Tian, A., Cui, J., Ren, P., and Wang, M., *Experimental and Numerical Investigation on the Anti-Penetration Performance of Metallic Sandwich Plates for Marine Applications*. Journal of Sandwich Structures & Materials, 2019. **22**(2): p.494-522.
17. Sun, C., Albustani, H., Phadnis, V.A., Nasr, M., Cantwell, W.J., and Guan, Z., *Improving the structural integrity of foam-core sandwich composites using continuous carbon fiber stitching*. Composite Structures, 2023. **324**: p., 117509.
18. Mocian, O., Constantinescu, D.M., and Indreş, A., *Assessment on Energy Absorption of Foam Core Sandwich Panels Under Low Velocity Impact*. Macromolecular Symposia, 2021. **396**(1).
19. Ozer, S., Haciyusufoglu, F., and Vural, E., *Experimental investigation of the effect of the use of nanoparticle additional biodiesel on fuel consumption and exhaust emissions in tractor using a coated engine*. Thermal Science, 2023. **27**(4): p. 3189–3197.
20. Vural, E., Özer, S., Özel, S., and Binici, M., *Analyzing the effects of hexane and water blended diesel fuels on emissions and performance in a ceramic-coated diesel engine by Taguchi optimization method*. Fuel, 2023. **344**: p. 128105.
21. Chen, D., Yang, J., and Kitipornchai, S., *Elastic buckling and static bending of shear deformable functionally graded porous beam*. Composite Structures, 2015. **133**: p. 54–61.
22. Yang, J., Chen, D., and Kitipornchai, S., *Buckling and free vibration analyses of functionally graded graphene reinforced porous nanocomposite plates based on Chebyshev-Ritz method*. Composite Structures, 2018. **193**: p. 281–294.
23. Wang, Y.Q., and Zhao, H.L., *Free vibration analysis of metal foam core sandwich beams on elastic foundation using Chebyshev collocation method*. Archive of Applied Mechanics, 2019. **89**(11): p. 2335–2349.
24. Garg, A., Chalak, H.D., Li, L., Belarbi, M.O., Sahoo, R., and Mukhopadhyay, T., *Vibration and Buckling Analyses of Sandwich Plates Containing Functionally Graded Metal Foam Core*. Acta Mechanica Solida Sinica, 2022. **35**(4): p. 1–16.
25. Touloukian, Y.S., *Thermophysical properties of high temperature solid materials*. Macmillan, 1967.
26. Kiani, Y., and Eslami, M.R., *An exact solution for thermal buckling of annular FGM plates on an elastic medium*. Composite Part B: Engineering, 2013. **45**(1): p.101–110.
27. Zhang, D.G., *Thermal post-buckling and nonlinear vibration analysis of FGM beams based on physical neutral surface and high order shear deformation theory*. Meccanica, 2014. **49**(2): p.283–293.
28. Eringen, A.C., *Theories of nonlocal plasticity*. International Journal of Engineering Science, 1983. **21**(7): p.741–751.
29. Lim, C.W., Zhang, G., and Reddy, J.N., *A higher-order nonlocal elasticity and strain gradient theory and its applications in wave propagation*. Journal of the Mechanics and Physics of Solids, 2015. **78**: p.298–313.
30. Farajpour, A., and Rastgoo, A., *Influence of carbon nanotubes on the buckling of microtubule bundles in viscoelastic cytoplasm using nonlocal strain gradient theory*. Results in Physics, 2017. **7**: p.1367–1375.
31. Eringen, A.C., *On differential equations of nonlocal elasticity and solutions of screw dislocation and surface waves*. Journal of Applied Physics, 1983. **54**(9): p.4703–4710.
32. Li, L., Li, X., and Hu, Y., *Free vibration analysis of nonlocal strain gradient beams made of functionally graded material*. International Journal of Engineering Science, 2016. **102**: p.77–92.
33. Żur, K.K., Arefi, M., Kim, J., and Reddy, J.N., *Free vibration and buckling analyses of magneto-electro-elastic FGM nanoplates based on nonlocal modified higher-order sinusoidal shear deformation theory*. Composite Part B: Engineering, 2020. **182**.
34. Aghababaei, R., and Reddy, J.N., *Nonlocal third-order shear deformation plate theory with application to bending and vibration of plates*. Journal of Sound and Vibration, 2009. **326**(1–2): p.277–289.
35. Monaco, G.T., Fantuzzi, N., Fabbrocino, F., and Luciano, R., *Critical temperatures for vibrations and buckling of magneto-electro-elastic nonlocal strain gradient plates*. Nanomaterials, 2021. **11**(1): p.1–18.
36. Ramirez, F., Heyliger, P.R., and Pan, E., *Discrete layer solution to free vibrations of functionally graded magneto-electro-elastic plates*. Mechanics of

Advanced Materials and Structures, 2006. **13**(3): p.249–266.

Appendix

The coefficient of the **S** and **M** matrices:

$$s_{11} = (A_{11}k_1^2 + A_{66}k_2^2)c_2, \quad s_{12} = (A_{12} + A_{66})k_1k_2c_2, \quad s_{13} = (-B_{11}k_1^3 - (B_{12} + 2B_{66})k_1k_2^2)c_2$$

$$s_{14} = (-B_{11}^s k_1^3 - (B_{12}^s)k_1k_2^2)c_2, \quad s_{15} = (-X_{13}k_1)c_2, \quad s_{22} = (A_{66}k_1^3 + A_{22}k_2^2)c_2$$

$$s_{23} = (-B_2k_2^3 - (B_{12} + 2B_{66})k_1^2k_2)c_2, \quad s_{25} = (-X_{23}k_2)c_2$$

$$s_{33} = \left(D_{11}k_1^4 + 2(D_{12} + 2D_{66})k_1^2k_2^2 + D_{22}k_2^4 + (-N^T)(k_1^2 + k_2^2)\right)c_1,$$

$$s_{34} = \left((-N^T)(k_1^2 + k_2^2)\right)c_1, \quad s_{55} = \left(A_{55}^s k_1^2 + A_{44}^s k_2^2 + Z_{33} + g(-N^T)(k_1^2 + k_2^2)\right)c_1$$

$$s_{35} = (Y_{13}k_1^2 + Y_{23}k_2^2)c_2, s_{44} = \left((-N^T)(k_1^2 + k_2^2)\right)c_1$$

$$m_{11} = I_0c_1, \quad m_{13} = -k_1I_1c_1, \quad m_{14} = -k_1J_1c_1, \quad m_{22} = I_0c_1, \quad m_{23} = -k_2I_1c_1, \quad m_{24} = -k_2J_1c_1$$

$$m_{33} = \left(I_0 + I_2(k_1^2 + k_2^2)\right)c_1, \quad m_{34} = \left(I_0 + J_1(k_1^2 + k_2^2)\right)c_1, \quad m_{35} = J_0c_1$$

$$m_{44} = \left(I_0 + K_2(k_1^2 + k_2^2)\right)c_1, \quad m_{45} = J_0c_1, \quad m_{55} = K_0c_1$$

$$c_1 = \left(1 + l_m^2(k_1^2 + k_2^2)\right) \quad c_2 = \left(1 + e_0a^2(k_1^2 + k_2^2)\right)$$